Available online at www.sciencedirect.com
ScienceDirect
Journal of Power Sources 164 (2007) 174–181
JOURNAL OF POWER SOURCES
www.elsevier.com/locate/jpowsour

A complete two-phase model of a porous cathode of a PEM fuel cell

J.J. Hwang *,[1]

Department of Environment and Energy, National University of Tainan, Tainan 700, Taiwan

Received 10 August 2006; received in revised form 1 October 2006; accepted 3 October 2006
Available online 28 November 2006

Abstract

This paper has developed a complete two-phase model of a proton exchange membrane (PEM) fuel cell by considering fluid flow, heat transfer and current simultaneously. In fluid flow, two momentum equations governing separately the gaseous-mixture velocity ($\mathbf{u}_g$) and the liquid-water velocity ($\mathbf{u}_w$) illustrate the behaviors of the two-phase flow in a porous electrode. Correlations for the capillary pressure and the saturation level connect the above two-fluid transports. In heat transfer, a local thermal non-equilibrium (LTNE) model accounting for intrinsic heat transfer between the reactant fluids and the solid matrices depicts the interactions between the reactant-fluid temperature (T_f) and the solid-matrix temperature (T_s). The irreversibility heating due to electrochemical reactions, Joule heating arising from Ohmic resistance, and latent heat of water condensation/evaporation are considered in the present non-isothermal model. In current, Ohm's law is applied to yield the conservations in ionic current ($\mathbf{i}_m$) and electronic current ($\mathbf{i}_s$) in the catalyst layer. The Butler–Volmer correlation describes the relation of the potential difference (overpotential) and the transfer current between the electrolyte (such as Nafion^{TM}) and the catalyst (such as Pt/C).

Keywords: Two-phase transport; Model; Porous electrode

1. Introduction

As illustrated in Fig. 1, three kinds of two-phase transport phenomena can be characterized in an operating proton exchange membrane (PEM) fuel cell. The first one is two-phase flow, i.e., $\mathbf{u}_w$ and $\mathbf{u}_g$. It is attributed to the morphological phase in water. Pressure difference between the liquid water and the gaseous mixture causes the capillary force that affects the saturation level in the porous electrode. The second one is two-phase temperature, i.e., T_f and T_s. Temperature difference between the reactant fluids and the solid matrices (i.e., carbon fibers) results in intrinsic heat transfer in the gas diffusion layer. The last one is two-phase current, i.e., $\mathbf{i}_m$ and $\mathbf{i}_s$. Potential difference between the electrolyte (such as Nafion^{TM}) and the catalyst (such as Pt/C) drives the transfer current inside the catalyst layer.

A large amount of research works about two-phase models of a PEM fuel cell have been proposed in the past few years. Only those most closely related to the present study are briefly cited below. Berning and Djilali [1] and Nam and Kaviany [2] modeled two-phase flow in a PEM fuel cell. Two-phase currents were not considered since the catalyst layer was treated as a thin interface. Zhou and Liu [3], Ju and Wang [4], and Lin and Nguyen [5] coupled two-phase current to two-phase flow under the adiabatic conditions. Hwang et al. [6–9] developed a local thermal non-equilibrium (LTNE) model to discuss the characteristics of two-phase temperature in a PEM fuel cell. The reactant fluids were assumed to be gaseous. Basically, all previous two-phase models discussed one or two of the aforementioned two-phase transports. None has provided a full coverage of the three two-phase transports so far. The objective of this work is to develop a complete two-phase that covers all two-phase components in a porous cathode of a PEM fuel cell, i.e., velocity (liquid water/gaseous mixture), temperature (reactant fluids/solid matrices), and current (ionic conductor/electronic conductor). This paper is the first step in developing a comprehensive two-phase model for a conventional PEM fuel cell cathode, which is believed to be of great importance in accurately describing the transport phenomena occurring in a PEM fuel cell.

2. Model description

A schematic drawing showing a two-layer cathode of a PEM fuel cell is given in Fig. 1. The humidified air diffuses into the

* Fax: +886 62600321.
E-mail address: azaijj@mail.nutn.edu.tw.
[1] Professor, and also research fellow of Fuel Cell Center of Yuan-Ze University.

0378-7753/$ – see front matter © 2006 Elsevier B.V. All rights reserved.
doi:10.1016/j.jpowsour.2006.10.045

Nomenclature

c	mole concentration of the species (mol m^{-3})
D_i	diffusivity of species i (m^2 s^{-1})
F	Faraday's constant (96,487 C mol^{-1})
h_v	interfacial heat transfer coefficient (volumetric) (W m^3 K^{-1})
$\mathbf{i}$	current density (A m^{-2})
j	transfer current density (A m^{-3})
k	thermal conductivity (W K^{-1} m^{-1})
$\dot{m}_{phase}$	phase change mass transfer (kg m^{-3} s^{-1})
$\dot{m}_{ORR,O_2}$	oxygen mass transfer rate due to oxygen reduction reaction (kg m^{-3} s^{-1})
$\dot{m}_{ORR,H_2O}$	water mass transfer rate due to oxygen reduction reaction (kg m^{-3} s^{-1})
M	molecular weight (kg mol^{-1})
p	pressure (Pa)
$\dot{q}$	heat flux (W m^{-3})
R	universal gas constant (W mol^{-1} K^{-1})
s	saturation
T	temperature (K)
$\mathbf{u}$	velocity vectors (m s^{-1})
x_j	mass fraction of the species j
x, y	coordinate system, Fig. 1 (m)

Greek symbols

α	symmetric factor
ε	porosity (gas diffusion layer)
ϕ	phase potential (V)
κ	permeability (m^2)
ρ	density (kg m^3)
σ	conductivity (Ω^{-1} m^{-1})
τ	tortuosity
ω	mass fraction

Subscripts

c	capillary or catalyst layer
eff	effective
f	fluid
g	gas phase
int	intrinsic
m	membrane (electrolyte) phase
ORR	oxygen reduction reaction
s	solid or catalyst phase
w	water
Ω	resistive loss

Superscript

sat	saturation

gas diffusion layer (GDL) and catalyst layer (CL) from the flow channel. Then, the oxygen reacts together with the protons to form liquid water in the catalyst layer. Meanwhile, the heat generation due to the overpotential and irreversibility heating during the electrochemical reaction is removed by either the reactant fluids or the solid matrices. The porous cathode is treated as homogeneous porous media with uniform morphological properties such as porosity and permeability. Typical data are list in Table 1.

2.1. Two-phase velocity

Two-phase flows in porous electrode follow separate equations for the gaseous mixture and liquid water:

$$\nabla(\rho_g \mathbf{u}_g) = \dot{m}_{ORR,O_2} - \dot{m}_{phase} \tag{1}$$

$$\nabla(\rho_w \mathbf{u}_w) = \dot{m}_{ORR,H_2O} + \dot{m}_{phase} \tag{2}$$

The first term on the right-hand side of above equations means a sink/source of oxygen/water during the oxygen reduction reaction (ORR). Since the reacting temperature of oxygen reduction reaction in the cathodic catalyst layer should be below 100 °C, the product water ($\dot{m}_{ORR,H_2O}$) is assumed to be in liquid phase. Through non-equilibrium evaporation ($-\dot{m}_{phase}$) of liquid water from the pre-existing liquid surface, water vapor is introduced diffusively into the porous medium. ρ_g and ρ_w are the densities of gaseous mixture and liquid water, respectively. The velocities of gaseous mixture and liquid water are expressed by the Darcy's law, i.e.,

$$\frac{1}{\varepsilon}\nabla\cdot(\rho \mathbf{u}_g \mathbf{u}_g) = -\varepsilon\nabla p_g + \nabla\cdot(\mu_g \nabla \mathbf{u}_g) - \frac{\varepsilon\mu \mathbf{u}_g}{\kappa k_{rg}} \tag{3}$$

$$\frac{1}{\varepsilon}\nabla\cdot(\rho \mathbf{u}_w \mathbf{u}_w) = -\varepsilon[\nabla p_c + (\rho_w - \rho_g)g] + \nabla\cdot(\mu_w \nabla \mathbf{u}_w) - \frac{\varepsilon\mu_w \mathbf{u}_w}{\kappa k_{rw}} \tag{4}$$

where κ_0 is the permeability of the dry electrode, while k_{rg} and k_{rw} are the relative permeabilities of the gaseous mixture and the liquid water, respectively. They account for the reduction in pore space available for one phase due to the existence of the second phase. In this work, we assume isotropic porous electrode with relative permeability of each individual phase preoperational to the cube of phase saturations, i.e., $k_{rg} = (1-s)^3$ and $k_{rw} = s^3$ [10].

The capillary forces due to the imbalance of the liquid-water pressure and the gaseous-mixture pressure can be expressed as

$$p_c = p_w - p_g \tag{5}$$

This shows the liquid-water pressure should be higher and makes it possible to transport liquid water out of the hydrophobic porous electrode without severe flooding, and also prevents wicking of water from the channels. The functional variation of capillary pressure with saturation is prescribed following Leverett [11]:

$$p_c(s) = p_w - p_g = \delta\left(\frac{\varepsilon}{\kappa_o}\right) f(s) \tag{6}$$

where δ is the interfacial liquid/gas tension; ε the porosity; $f(s)$ is the empirical function proposed by Udell [12]:

$$f(s) = 1.42(1-s) - 2.12(1-s)^2 + 1.26(1-s)^3 \tag{7}$$

The interfacial mass-transfer rate between the gas and liquid phases $\dot{m}_{phase}$ is assumed to be proportional to the amount of the reactant in the porous media and the difference between

Components	Gas diffusion layer (GDL)	Catalyst layer (CL)
Velocity	Two-phase, $\mathbf{u}_g$, $\mathbf{u}_w$	Two-phases, $\mathbf{u}_g$, $\mathbf{u}_w$
Temperature	Two-phase, T_s T_f	Single-phase, $T_s = T_f$
Current	Single-phase, $\mathbf{i}_s$	Two-phase, $\mathbf{i}_s$, $\mathbf{i}_m$

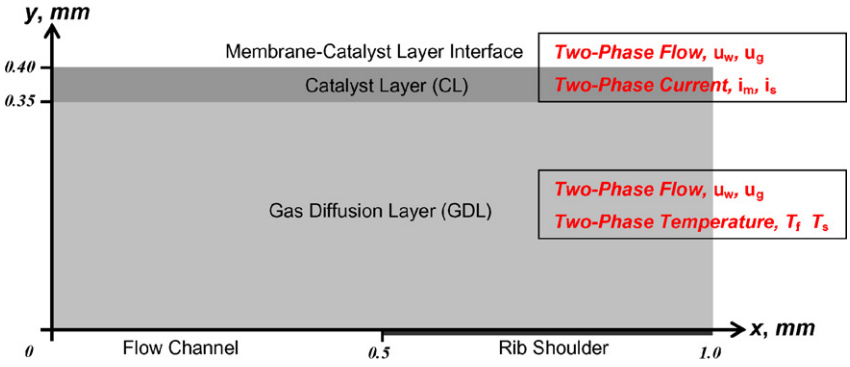

Fig. 1. Schematic drawing of model domain of a two-layer porous cathode.

water-vapor partial pressure (p_{H_2O}) and its saturation pressure ($p^{sat}_{H_2O}$), i.e. [2,13],

$$\dot{m}_{phase} = \begin{cases} k_{con}\varepsilon(1-s)x_{H_2O}\dfrac{(p_{H_2O}-p^{sat}_{H_2O})}{RT_f} & \text{if } p_{H_2O}-p^{sat}_{H_2O} \geq 0 \\ k_{evp}\varepsilon s\dfrac{\rho_w}{M_{H_2O}}(p_{H_2O}-p^{sat}_{H_2O}) & \text{if } p_{H_2O}-p^{sat}_{H_2O}<0 \end{cases} \quad (8)$$

The upper half represents the condensation rate while the lower half represents the evaporation rate. k_{con} and k_{evp} are the condensation and evaporation rate constants, respectively [13]. x_{H_2O} is the mole fraction of water vapor. The saturation pressure of water, $p^{H_2O}_{sat}$ is a function of the operating temperature (T_f), which is read directly from the steam tables.

2.2. Two-phase temperature

A local thermal non-equilibrium model [8] is used to describe the two-phase temperatures in the porous electrode. The energy equations for solid matrices and reactant fluids in the GDL are,

Table 1
Porous-electrochemical properties of the present modeled fuel cell

Name	Description	Value
$c_{O_2,ref}$	Reference mole fraction of oxygen (mol m^{-3})	3.6641
$c_{H_2O,ref}$	Reference mole fraction of water (mol m^{-3})	0.0703
i_0	Exchange current density (A m^{-2})	5.0×10^{-4}
Sa	Surface area to volume ratio (m^{-1})	1000
j_0	(Volumetric) exchange current density (A m^{-3})	0.5
ε	Porosity	0.45
κ_0	Absolute permeability (m^2)	2.55×10^{-13}
h_v	Intrinsic heat transfer coefficient (W m^{-3} K^{-1})	1×10^5
σ_m	Ionic conductivity (electrolyte phase) (Ω^{-1} m^{-1})	14.4
σ_s	Electronic conductivity (catalyst phase) (Ω^{-1} m^{-1})	300
k_{cs}	Solid-phase thermal conductivity in the catalyst layer (W kg^{-1} K^{-1})	1.1
$k_{s,eff}$	Solid thermal conductivity (W kg^{-1} K^{-1})	1.7
$k_{f,eff}$	Fluid thermal conductivity (W kg^{-1} K^{-1})	0.051
$k_{c,eff}$	Catalyst layer thermal conductivity (W kg^{-1} K^{-1})	0.656
k_l	Electrolyte thermal conductivity (W kg^{-1} K^{-1})	0.5
$c_{p,f}$	Reactant-fluids thermal capacity (J kg^{-1} K^{-1})	1006
$c_{p,s}$	Solid thermal capacity (J kg^{-1} K^{-1})	885
ρ_s	Solid-part density (kg m^{-3})	1100
ρ_l	Electrolyte (Nafion 117) density (kg m^{-3})	1960
ρ_w	Water density (kg m^{-3})	1000
μ_w	Water viscosity (Pa s)	3.65×10^{-4}
ε_{GDL}	Porosity of gas diffusion layer	0.48
ε_{CL}	Porosity of catalyst layer	0.42
k_{evp}	Evaporation rate constant (atm^{-1} s^{-1})	100
k_{con}	Condensation rate constant (s^{-1})	100
$\omega_{H_2O,in}$	Inlet water-vapor mass fraction	0.0198
$\omega_{O_2,in}$	Inlet oxygen mass fraction	0.2284
$\omega_{N_2,in}$	Inlet nitrogen mass fraction	0.7518

Table 2
Source terms of the two-phase equations

Equations	Source term	Gas diffusion layer (GDL)	Catalyst layer (CL)
Momentum	$\dot{m}_{\mathrm{ORR,O_2}}$	0	$-j_{\mathrm{ct}}M_{\mathrm{O_2}}/(4F)$
	$\dot{m}_{\mathrm{ORR,H_2O}}$	0	$j_{\mathrm{ct}}M_{\mathrm{H_2O}}/(2F)$
	$\dot{m}_{\mathrm{phase}}$	Eq. (8)	Eq. (8)
Energy	$\dot{q}_{\Omega}$	$\mathbf{i}_{\mathrm{s}}^2/\sigma_{\mathrm{s,eff}}$	$\mathbf{i}_{\mathrm{m}}^2/\sigma_{\mathrm{m,eff}}+\mathbf{i}_{\mathrm{s}}^2/\sigma_{\mathrm{s,eff}}$
	$\dot{q}_{\mathrm{phase}}$	$\dot{m}_{\mathrm{phase}}\times h_{\mathrm{fg}}$	$\dot{m}_{\mathrm{phase}}\times h_{\mathrm{fg}}$
	$\dot{q}_{\mathrm{int}}$	$h_{\mathrm{v}}\times(T_{\mathrm{s}}-T_{\mathrm{f}})$	0
	$\dot{q}_{\mathrm{ORR}}$	0	$j_{\mathrm{ct}}\times(\phi_{\mathrm{m}}-\phi_{\mathrm{m}})$
Charge	s_j	0	j_{ct}

respectively, represented by the following forms [14].

$$\nabla\cdot(-k_{\mathrm{s,eff}}\nabla T_{\mathrm{s}})=-\dot{q}_{\mathrm{int}}+\dot{q}_{\Omega} \tag{9}$$

$$(\rho c_{\mathrm{p}})_{\mathrm{f}}\mathbf{u}\cdot\nabla T_{\mathrm{f}}+\nabla\cdot(-k_{\mathrm{eff}}\nabla T_{\mathrm{f}})=\dot{q}_{\mathrm{int}}+\dot{q}_{\mathrm{phase}} \tag{10}$$

where $k_{\mathrm{s,eff}}$, and $k_{\mathrm{f,eff}}$, are the effective thermal conductivities of solid matrices and reactant fluids, respectively. In Eq. (9) (solid-phase temperature), the source terms $\dot{q}_{\Omega}$ and $\dot{q}_{\mathrm{int}}$ stand for the Joule heating and intrinsic heat transfer between the solid-matrices and the reactant fluids, respectively. They are provided in Table 2. In the fluid-phase energy equation (Eq. (10)), the phase-change heat transfer, $\dot{q}_{\mathrm{phase}}$, can be represented by the product of the latent heat of evaporation/condensation (h_{fg}) and the interfacial mass transfer rate ($\dot{m}_{\mathrm{phase}}$), i.e.,

$$\dot{q}_{\mathrm{phase}}=\dot{m}_{\mathrm{phase}}\times h_{\mathrm{fg}} \tag{11}$$

Basically, the quantity $\dot{q}_{\mathrm{phase}}$ is strongly dependent on the fluid-phase temperature. First, the latent heat of phase change is a function of the fluid temperature, i.e., $h_{\mathrm{fg}}(T_{\mathrm{f}})$. Secondly, if condensation occurs, the quantity $\dot{m}_{\mathrm{phase}}$ will be positive; thus, $\dot{q}_{\mathrm{phase}}>0$. That is condensation will heat up the control volume. An increase in the fluid-phase temperature will increase the saturation pressure of water. Thus, the driving force for condensation ($p_{\mathrm{H_2O}}-p_{\mathrm{H_2O}}^{\mathrm{sat}}$) will decrease, resulting in a decrease of condensation rate. A similar argument also applies to evaporation. Note that the density of the reactant fluids is expressed by the average value of gas-phase mixture and the liquid water, i.e., $\rho_{\mathrm{f}}=\rho_{\mathrm{w}}s+\rho_{\mathrm{g}}(1-s)$.

In the catalyst layer, physically, the electrochemical reaction takes place at the interface of reactant fluid and catalyst under a fixed temperature. Therefore, the reactant fluids and the solid matrices have the same temperatures.

$$T_{\mathrm{f}}=T_{\mathrm{s}} \tag{12}$$

$$(\rho c_p)_{\mathrm{f}}\mathbf{u}\cdot\nabla T_{\mathrm{f}}+\nabla\cdot(-k_{\mathrm{c,eff}}\nabla T_{\mathrm{f}})=\dot{q}_{\mathrm{ORR}}+\dot{q}_{\Omega}+\dot{q}_{\mathrm{phase}} \tag{13}$$

where $k_{\mathrm{c,eff}}$, is the effective thermal conductivity of the catalyst layer [6]. The irreversiblility heating by the oxygen reduction reaction is expressed as $\dot{q}_{\mathrm{ORR}}=j_{\mathrm{ct}}(\phi_{\mathrm{m}}-\phi_{\mathrm{s}})$.

2.3. Two-phase current

In the catalyst layer, a potential difference between the electrolyte and catalyst drives the transfer current that keeps the electrochemical reaction continuously. The current passes through the catalyst layer can be decomposed into two parts, i.e., ionic currents ($\mathbf{i}_{\mathrm{m}}$) and electronic currents ($\mathbf{i}_{\mathrm{s}}$), respectively. Since the electrodes are electroneutral everywhere, there is no charge-buildup in the catalyst layers. Thus, the charge conservation is

$$\nabla\cdot(\mathbf{i}_{\mathrm{s}}+\mathbf{i}_{\mathrm{m}})=0 \tag{14}$$

These two currents interact through electrochemical reactions. The electrons are transferred to the electrolyte from the catalyst in the cathodic catalyst layer. Application of the Ohm's law to the equation yields the current conservation:

$$\nabla\cdot(-\sigma_{\mathrm{s,eff}}\nabla\phi_{\mathrm{s}})=j_{\mathrm{ct}} \tag{15}$$

$$\nabla(-\sigma_{\mathrm{m,eff}}\nabla\phi_{\mathrm{m}})=-j_{\mathrm{ct}} \tag{16}$$

where the source term j_{ct}, the local transfer current density corresponds to the oxygen reduction reaction in the catalyst layer. $\sigma_{\mathrm{s,eff}}$ and $\sigma_{\mathrm{m,eff}}$, are the effective electronic and ionic conductivities of the catalyst and electrolyte, respectively. They are modeled as

$$\sigma_{\mathrm{s,eff}}=\sigma_{\mathrm{s}}(1-\varepsilon_{\mathrm{c}})\times v_{\mathrm{s}}\times p_{i,\mathrm{s}} \tag{17}$$

$$\sigma_{\mathrm{m,eff}}=\sigma_{\mathrm{m}}(1-\varepsilon_{\mathrm{c}})\times v_{\mathrm{m}}\times p_{i,\mathrm{m}} \tag{18}$$

where v_{s} and v_{m} are the volume fractions of catalyst and electrolyte in the catalyst layer, respectively. $p_{i,\mathrm{s}}$, and $p_{i,\mathrm{m}}$, are the connectivities of catalyst and electrolyte in the catalyst layer, respectively. It is noted that only a long-range connection of the same particles stretch from the catalyst layer to the electrolyte ensures good conductivity.

2.4. Multi-species transports

The present model accounts for three species in the porous cathode, i.e., oxygen, water vapor and nitrogen. The species transports based on the Stefan–Maxwell multi-component diffusion are given by the following equations:

$$\rho_{\mathrm{g}}\mathbf{u}\cdot\nabla\omega_{\mathrm{O_2}}=\nabla\cdot\left\{\rho_{\mathrm{g}}\omega_{\mathrm{O_2}}\sum_{j=1}^{N}D_{ij}\left[\frac{M}{M_j}\left(\nabla\omega_j+\omega_j\frac{\nabla M}{M}\right)+(x_j-\omega_j)\frac{\nabla p}{p}\right]\right\}+S_{\mathrm{O_2}} \tag{19}$$

$$\rho_{\mathrm{g}}\mathbf{u}\cdot\nabla\omega_{\mathrm{H_2O}}=\nabla\cdot\left\{\rho_{\mathrm{g}}\omega_{\mathrm{H_2O}}\sum_{j=1}^{N}D_{ij}\left[\frac{M}{M_j}\left(\nabla\omega_j+\omega_j\frac{\nabla M}{M}\right)+(x_j-\omega_j)\frac{\nabla p}{p}\right]\right\}+S_{\mathrm{H_2O}} \tag{20}$$

$$\omega_{\mathrm{N_2}}=1-\omega_{\mathrm{O_2}}-\omega_{\mathrm{H_2O}} \tag{21}$$

The effective diffusivities of the three species in the porous cathode follow the Bruggemann model. The source terms for the

mass balances of oxygen and water vapor are, respectively, given by

$$S_{O_2} = \dot{m}_{ORR,O_2} \tag{22}$$

$$S_{H_2O} = -\dot{m}_{phase} \tag{23}$$

The local transfer current density is depicted by the Butler–Volmer correlation, i.e.,

$$j_{ct} = j_0 \left\{ \left(\frac{c_{O_2}}{c_{O_2,ref}} \right) \exp\left[\frac{4\alpha F}{RT_f}(\phi_m - \phi_s) \right] - \left(\frac{c_{H_2O}}{c_{H_2O,ref}} \right)^2 \times \exp\left[\frac{-4(1-\alpha)F}{RT_f}(\phi_m - \phi_s) \right] \right\} \tag{24}$$

where α is the symmetric factor and R is the universal gas constant. c_{O_2} and c_{H_2O} are the concentrations of oxygen and water vapor, respectively. $\phi_m - \phi_s$ is the difference of ionic potential and electronic potential in the porous electrode (i.e., overpotential). It drives the transfer current density from the electrolyte phase to the catalyst phase that keeps the electrochemical reaction continuously.

2.5. Boundary conditions and numerical methods

The electrochemical and physical properties used in the calculation are given in Table 1. At the module inlet, i.e., the interface between the GDL and the flow channel, the concentrations of gaseous species are 22.84%/1.98%/75.18% for $O_2/H_2O/N_2$, where N_2 is considered as an inert gas and serves as diluents. In addition, the temperatures for cathode feeds are fixed at 298 K. At the interface between the GDL and the rib-shoulder, all species fluxes are set to zero and the temperatures are fixed at 298 K. The solid potential at this interface is arbitrarily chosen to be zero. At the interface between the GDL and the CL, the electronic current and the fluxes of gaseous species and liquid water are continuous, while ionic current is set to zero. At the interface between the catalyst layer and the membrane, species and heat fluxes are set to zero and the water vapor is saturated. In addition, the total overpotential is used as boundary condition. For the rest of the boundaries, we have either insulation or symmetry conditions.

The governing equations are numerically solved by the finite-element method [6–9]. Solutions are considered to be converged at each test condition after the ratio of residual source (including mass, momentum, species, and charge) to the maximum flux across a control surface becomes below 1.0×10^{-6}. A total of 8682 unstructured meshes were used in the computational domain, with a fine mesh in the reaction region. The iterations proceeded until the change in the calculated airflow rate between 20 consecutive iterations was less than 0.1%. In order to achieve that, the necessary number of iterations varied between 300 and 1000. A typical simulation requires about 60 min of central processing unit time on a Pentium IV PC (2.8 GHz, 2 GB RAM) using Windows XP platform.

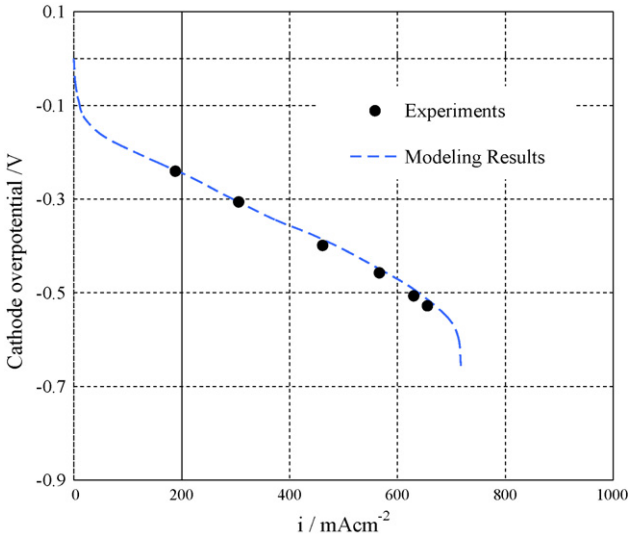

Fig. 2. Comparison of model results to experimental data.

3. Results and discussion

Before the subsequent discussion of the present results, it requires to validate the present model by comparing the present predictions with the experimental data. To this aim, a comparison of the cathode overpotential between the model results and the experimental data is made. Fig. 2 shows the experimental results in terms of the cathode half-cell overpotentials, and the model fit to the cathode side. The experimental data (solid circles) were determined by subtracting the activation overpotential for hydrogen oxidation on platinum [12] and the Ohmic loss in the membrane from the data obtained for the single-cell test. As seen in Fig. 2, the model results agree well with experimental data.

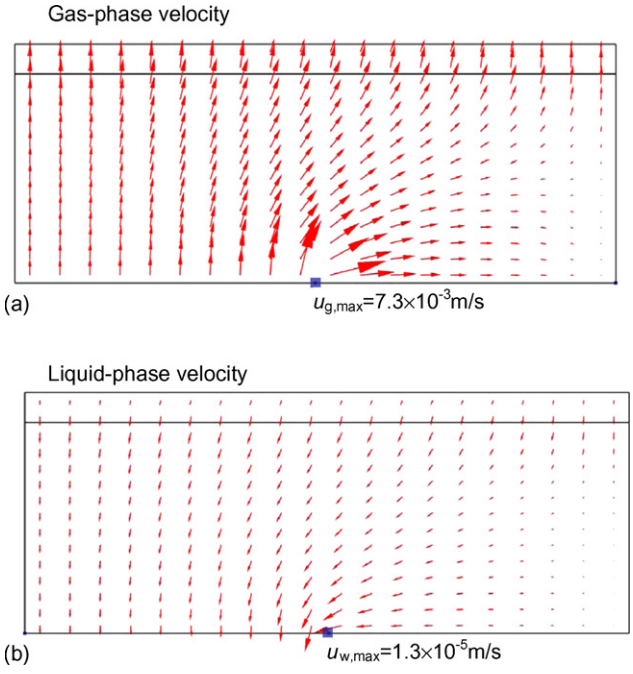

Fig. 3. Comparison of gas-phase and liquid-phase velocity distributions.

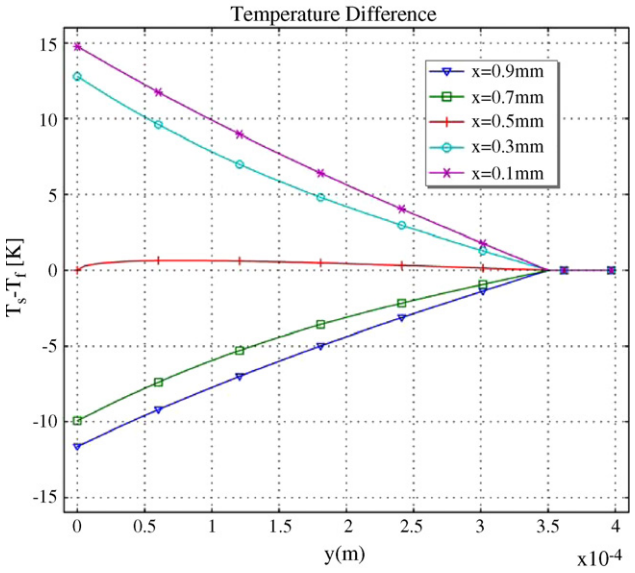

Fig. 4. Phase temperature differences at several x stations.

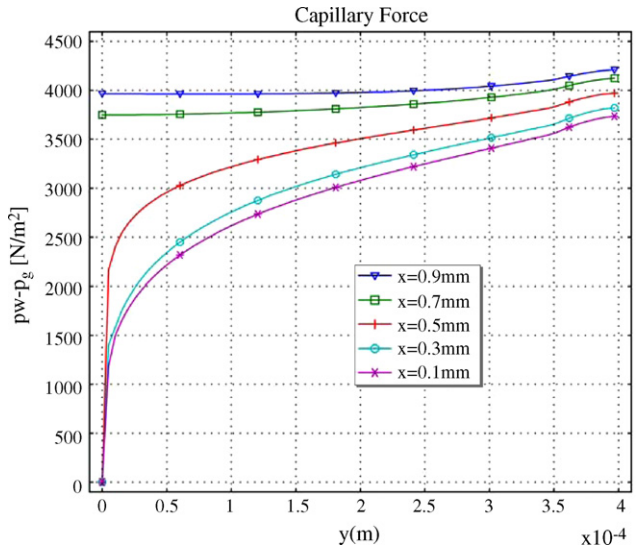

Fig. 5. Capillary forces at several x stations.

Fig. 3 shows the two-phase velocities inside the porous cathode. The gas-phase velocity vectors shown in Fig. 3(a) induce the gaseous mixture from the flow channel into the porous cathode. This is in contrast with the results obtained by the single-phase model [9] in which the gaseous-mixture velocity is directed from the porous cathode to the flow channel. As for the liquid-water velocity (Fig. 3(b)), it is opposed to the direction of gaseous mixture, i.e., with a direction from the cathode into the channel. As denoted in Fig. 3(a) and (b), the maximum velocities of gaseous mixture and liquid water are 7.3×10^{-3} and 1.3×10^{-5} m s^{-1}, respectively. They occur under the elbow of the rib-shoulder land.

As noted before, there are three kinds of two-phase transports, velocity, temperature and current occurring in an acting porous electrode. The interactions between two phases are intrinsic heat transfer, capillary force, and electrochemical reactions, respectively. Figs. 4–6 show the driving forces of the above two-phase transports. Fig. 4 shows the temperature difference between the solid phase and the fluid phase. In the catalyst layer, the reactant fluids and the solid matrices have the same temperature. Near the channel inlet, the solid-phase temperature is higher than the fluid-phase temperature, while an adverse trend is found near the rib-shoulder. The distribution of capillary force along several x stations in the porous cathode is shown in Fig. 5. The liquid saturation is higher in the catalyst layer, due to water generation, than the GDL-flow channel interface. Therefore, the capillary force gradient form in the porous electrode drives the liquid water from the reaction site to the open channel. Fig. 6 shows the potential difference between the ionic conductor (ϕ_l) and the electronic conductor (ϕ_s) in the catalyst layer. The phase potential increases along the depth (y) of the catalyst layer because of the decrease of oxygen concentration. In addition, the phase potential difference is higher in the region beneath the rib-shoulder but is lower in the region near the flow channel.

In the porous cathode, the essential parameter for determining the direction of phase change is the relative humidity (RH) of the gaseous mixture, i.e., the ratio of partial pressure of the water vapor in the gaseous mixture to the saturation pressure.

$$\mathrm{RH} = \frac{p_{\mathrm{H_2O}}}{p^{\mathrm{sat}}_{\mathrm{H_2O}}} = \frac{x_{\mathrm{H_2O}} \times p_{\mathrm{g}}}{p^{\mathrm{sat}}_{\mathrm{H_2O}}} \tag{25}$$

When the relative humidity exceeds 100%, it gives rise to condensation. On the other hand, evaporation occurs when the relative humidity is below 100% in the presence of liquid water. The phase-change mechanisms in a porous cathode of a PEM fuel cell are quiet complicated since all three parameters on the right-hand side of Eq. (25) vary [1]. They are competing in the directions of phase change and are described as follows. The oxygen reduction reaction in the cathodic catalyst layer will

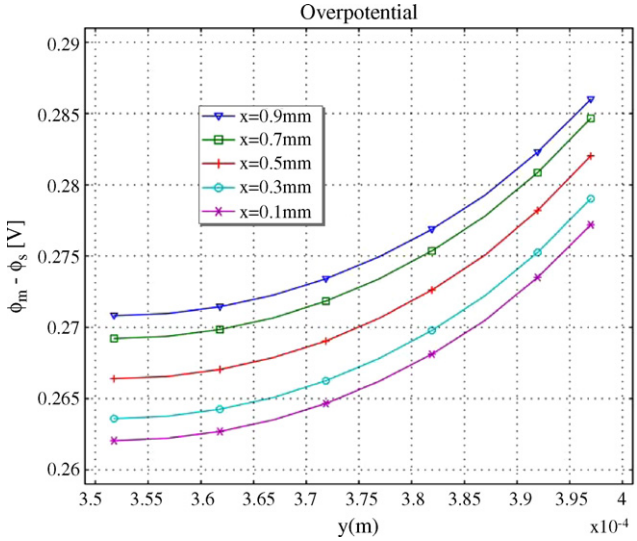

Fig. 6. Overpotential (phase-potential difference) distributions at several x stations.

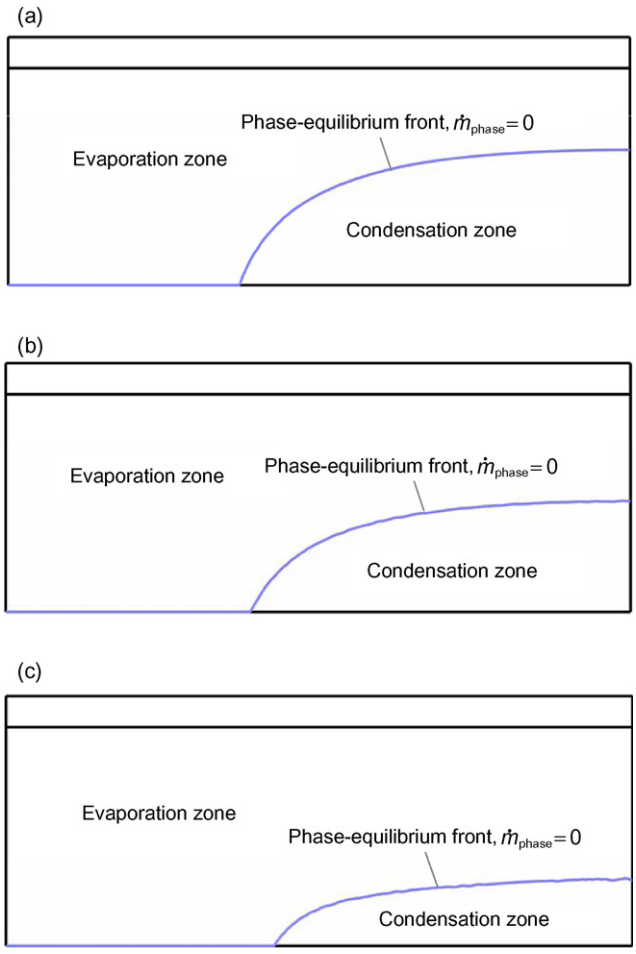

Fig. 7. Effect of rib-shoulder temperature (T_{rib}) on the adiabatic front of phase-change in the porous cathode of a PEM fuel cell: (a) $T_{rib}=298$ K; (b) $T_{rib}=308$ K; (c) $T_{rib}=318$ K.

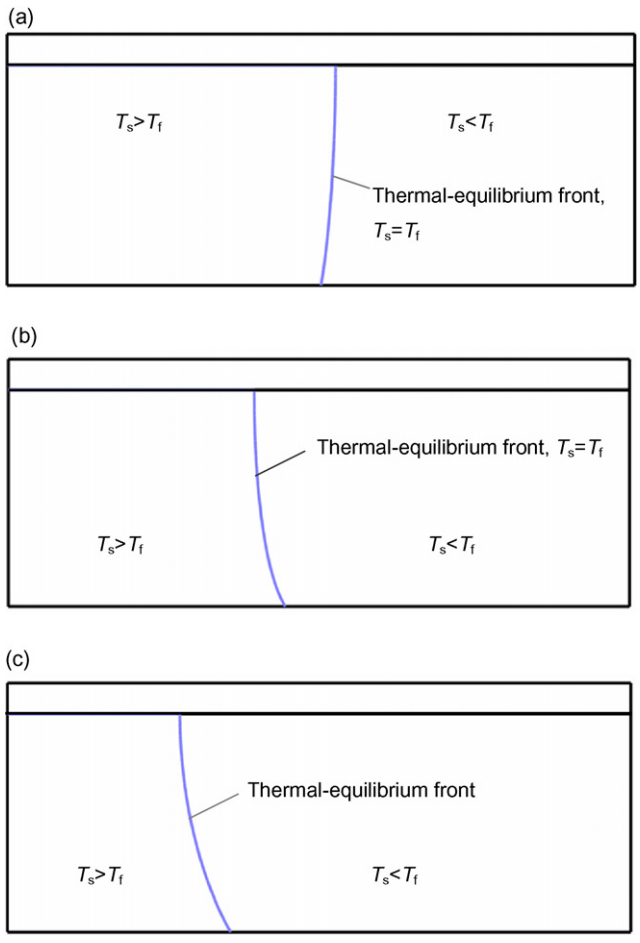

Fig. 8. Effect of rib-shoulder temperature (T_{rib}) on the thermally adiabatic front in the porous cathode of a PEM fuel cell: (a) $T_{rib}=298$ K; (b) $T_{rib}=308$ K; (c) $T_{rib}=318$ K.

increase the molar fraction of water vapor x_{H_2O}, simply due to the reactant consumption. Meanwhile, it also reduces the thermodynamic pressure of the gaseous mixture p_g. The combination of the two effects can lead to either evaporation or condensation. In addition, the exothermic reaction in the catalyst layer increases the fluid-phase temperature that increases the saturation pressure $p^{sat}_{H_2O}(T_f)$. It was found with an earlier version of this model that the fluid temperature can rise as high as 20 K [9], depending on the applied loading. This effect alone would lead to evaporation of liquid water.

The net phase change is a result of the balance among these competing, coupled, and spatially varying mechanisms. Fig. 7(a)–(c) shows the phase-change characteristics inside the porous cathode for several rib-shoulder temperatures. In each plot, a phase-equilibrium front divides the porous cathode into two regimes, i.e., the evaporation zone and the condensation zone, respectively. Above the front, the liquid water evaporates due to higher fluid-phase temperature than the inlet temperature. In the region below the front and above the rib-shoulder, the water vapor is condensed due to the decrease in fluid-phase temperature adjacent the cool rib-shoulder boundary. When the rib-shoulder temperature increases (T_{rib}), the condensation zone reduces, as shown in Fig. 7(b) and (c). Increasing the rib-shoulder temperature increases the nearby fluid-phase temperature that increases the saturation pressure. Thus, it is difficult to condense the water vapor in this region.

Fig. 8 shows the effect of the rib-shoulder temperature on the location of the thermal-equilibrium front in the porous cathode. On the right-hand side of the front, the fluid-phase temperature is higher than the solid-phase temperature. Conversely, the fluid-phase temperature is higher than the solid-phase temperature on the other site. It is seen that the thermal-equilibrium front is pushed leftward as the rib-shoulder temperature is increased.

4. Summary and conclusions

A two-phase model simultaneously considers velocity, temperature, and current in a PEM fuel cell has been developed in the present study. The three categories of two-phase transports are strongly coupled in an operating fuel cell. The unique feature of the present model is to successfully predict the phase-equilibrium front and the thermal equilibrium front in a porous cathode of a PEM fuel cell, which allows for a more realistic spatial variation of two-phase parameters. Results show that increasing the rib-shoulder temperature will reduces the con-

densation zones. This is because the hot rib-shoulder surfaces increase the nearby fluid-phase temperature that increases the saturation pressure; thus, it is difficult to condense the water vapor in this region.

In addition to an investigation of the effects of permeability and wetting characteristics of the porous cathode, future work will focus on incorporating membrane transport and fully coupling the anode and cathode transport, as well as on implementing more efficient numerical strategies, including parallel computing to allow practical use of the model for systematic parametric studies.

Acknowledgment

This research was partly sponsored by the National Science Council of Taiwan under contract no. NSC 92-2212-E-451-002.

References

[1] T. Berning, N. Djilali, J. Electrochem. Soc. 150 (2003) A1589.
[2] J.H. Nam, M. Kaviany, Int. J. Heat Mass Transfer 46 (2003) 4595.
[3] T. Zhou, H. Liu, J. Power Sources 138 (2004) 101.
[4] H. Ju, C.Y. Wang, J. Electrochem. Soc. 151 (2004) A1954.
[5] G. Lin, T.V. Nguyen, J. Electrochem. Soc. 153 (2006) A372.
[6] J.J. Hwang, J. Electrochem. Soc. 153 (2006) A216.
[7] J.J. Hwang, ASME J. Heat Transfer 128 (2006) 434.
[8] J.J. Hwang, P.Y. Chen, Int. J. Heat Mass Transfer 49 (2006) 2315.
[9] J.J. Hwang, C.H. Chao, W.Y. Ho, C.L. Chang, D.Y. Wang, J. Power Sources 157 (2006) 85.
[10] M. Kaviany, Principles of Heat Transfer in Porous Media, 2nd ed., Springer, New York, 1999.
[11] M.C. Leverett, Trans. Am. Inst. Min., Metall. Pet. Eng. 142 (1941) 152.
[12] K.S. Udell, Int. J. Heat Mass Transfer 28 (1985) 485.
[13] W. He, J.S. Yi, T.V. Nguyen, AIChE J. 46 (2000) 2053.
[14] J.J. Hwang, G.J. Hwang, R.H. Yeh, C.H. Chao, J. Heat Transfer 124 (2002) 120.